TIP-LEAKAGE VORTEX INCEPTION ON A DUCTED ROTOR

Carolyn Q. Judge, Ghanem F. Oweis, Steven L. Ceccio
University of Michigan
Ann Arbor, MI, USA

Stuart D. Jessup, Christopher J. Chesnakas, David J. Fry
Naval Surface Warfare Center - Carderock Division
Carderock, MD, USA

Abstract

The tip-leakage vortex occurring on a ducted rotor was examined using both three component Laser Doppler Velocimetry (LDV) and planar Particle Imaging Velocimetry (PIV). The vortex strength and core size were examined for different vortex cross sections downstream of the blade trailing edge. The variability of these quantities are observed with PIV and the average quantities are compared between LDV and PIV. Developed cavitation is also examined for the leakage vortex. The implication of vortex variability on cavitation inception is discussed.

1 Introduction

Tip-vortex cavitation is a source of noise, propeller-induced hull vibration and erosion of downstream rudders. With a ducted propeller, the tip clearance vortex can cause damage to the duct surface as well. The pressure difference across the two sides of the blade along with the presence of a gap between the duct and propeller blade result in a tip clearance or leakage flow. The leakage flow interacts with the through-flow across the suction side of the blade to form a sheet of vorticity that rolls up into a tip clearance vortex. Tip-vortex cavitation occurs when the pressure in the core of this vortex drops below vapor pressure and small bubbles within the vortex core begin to explosively grow. With further decreases in pressure, the core of the vortex can fill with vapor.

Researchers have examined the flow of tip and leakage vortices in order to determine when cavitation will occur and to develop predictive scaling laws. Recent studies of tip-vortex cavitation are reviewed by Fruman *et al.*(1992), Fruman *et al.*(1995), and Maines and Arndt (1997). Research on leakage-vortex cavitation is more limited, and a recent review is given by Boulon *et al.* (1999). Of particular note is the study of Farrell and Billet (1994) where the scaling of leakage vortex inception was presented.

Scaling of vortex cavitation inception often follows the idea of McCormick (1962) whereby the pressure within the core of the vortex can be related to the viscous flow over the lifting surface and the lift that the surface produces. If axisymmetric vortex flow is assumed, the local depression of pressure at the center of the vortex is proportional to the circulation of the vortex and the size of the viscous vortex core. McCormick assumed that the core size is proportional to the mean boundary layer thickness on the lifting surface, and that the vortex circulation was proportional to the lift coefficient, C_L. Reynolds number dependence arises from the assumption that the boundary layer thickness grows as $Re^{1/5}$. Lastly, it is assumed that the vortex will cavitate when the core pressure falls below vapor pressure. When combined, these relations lead to the scaling:

$$\sigma \approx C_L^2 Re^{2/5}. \tag{1}$$

This scaling has been successfully used to determining the point of cavitation desinence across Reynolds numbers. Scaling of cavitation inception must also include the effect of both the dissolved and free gas content

in the flow. Farrell and Billet (1994) discuss how McCormick scaling should be modified for application to tip-leakage flows, especially with regard to the choice of scaling for the core size with varying tip clearance.

While the above scaling has proven useful and predictive, there are features of tip-vortex flows that are not directly captured. These include the dynamics of the vortex during roll-up near the point of vortex formation, the effect of secondary vorticity in the roll-up region, the influence of axial flow within the vortex core, and the effect of turbulence near and within the core (Pauchet, 1997). For tip-leakage flows, there is the added influence flow near the shroud.

We wish to examine the process of tip-leakage vortex cavitation inception and its scaling as it occurs on a ducted rotor. Our overall goal will be to determine what physical processes are at work within the flow field to lead to the inception of discreet cavitation events. As in previous studies of vortex cavitation inception, we will examine the flow field using three-component Laser Doppler Velocimetry (LDV). LDV provides time-averaged measurements of the three-dimensional flow-field with relatively high spatial resolution. However, it is well known that global unsteadiness of the vortex flow field ("vortex wandering") can lead to erroneous interpretation of average flow fields, especially with regard to the estimation of turbulent flow quantities (Straka and Farrell, 1992). Consequently, we have combined the LDV measurements with instantaneous velocity field measurements acquired with planar Particle Imaging Velocimetry (PIV) to examine the variability in the vortical flow. Tip-vortex cavitation and near-tip velocity distributions were measured on a three-bladed propeller designated "Propeller 5206". The tests were performed in the NSWCCD 36-inch water tunnel. Presented here are some preliminary results of this study and an accompanying discussion of their implications.

2 Experimental Setup

Water Tunnel All measurements were made in the David Taylor 36-inch Variable Pressure Water Tunnel. The tunnel is a recirculating design with interchangeable test sections. (See Brownell, 1962, for a detailed description of the water tunnel). The 36-inch diameter, open jet test section was used for these tests. For these test, the propeller was driven using the upstream dynamometer. Inflow to the propeller was uniform except for the wakes from three upstream shaft support struts.

Propeller Model Propeller 5206 is a three bladed rotor designed to operate in a cylindrical duct. The duct in this case is a cylindrical extension of the NSWCCD 36-inch water tunnel flow nozzle. This configuration produces an inner duct diameter of 0.8636 m (34 inches), the largest propeller operated in the 36-inch water tunnel. The rotor can be operated at speeds up to 500 rpm resulting in blade Reynolds Numbers on the order of 1/4 of full scale.

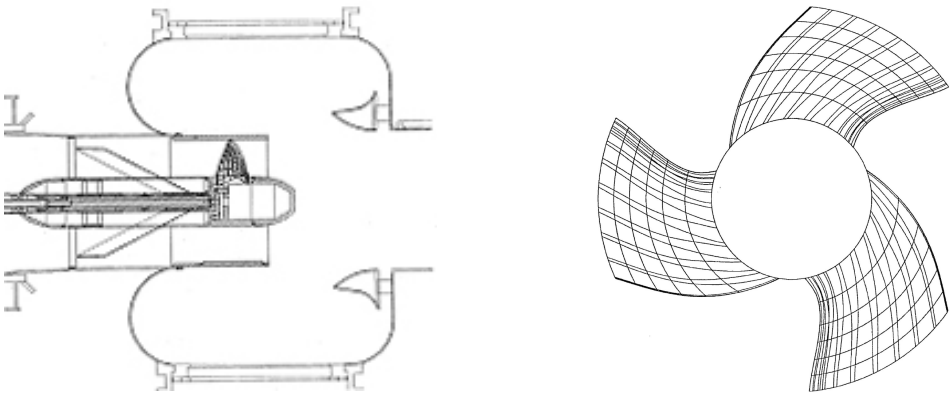

Figure 1: Propeller 5206 in the 36-inch water tunnel at the Naval Surface Warfare Center, Carderock Division and a view of the propeller along the shaft axis

The rotor has a diameter of 0.8504 m (33.475 inches), maintaining a $0.015R_P$ (Radius $R_P = 0.4252$ m) tip clearance resulting in a 6.67 mm (0.2625 in) tip gap. The blade chord-length is a constant 0.381 m (15 in) across the span. Blade thickness approaches 10% of chord at the tip. The tip geometry is simple with a

constant 3.175 mm (1/8 in) radius wrapped about the tip. The ratio of the tip clearance to the maximum thickness at the tip is 0.17, which is near the optimum value of 0.2 reported by Farrell and Billet (1994). The propeller was made using a numerically controlled milling process and manufactured to tolerances of approximately 0.1 mm (0.004 in) from a monobloc 6061T6 aluminum forging. The blade section is a NACA 66, DTMB (David Taylor Model Basin) modified thickness form, with $a = 0.8$ meanline camber, with trailing edges thickened to incorporate a typical anti-singing trailing edge bevel. The blade pitch was reduced at the hub and tip to minimize root and tip cavitation. Table 1 summarizes the blade geometry. Figure 2 shows the test setup with the propeller, duct, LDV and PIV systems as well as the trajectory of the developed cavitating vortex.

Table 1. Propeller 5206 Blade geometry description.

r/R_P	C/D	P/D	I_T/D	T/C	F/C	$\theta_s, Degrees$
0.416	0.446	0.92	-0.0063	0.172	-0.065	-0.4
0.5	0.446	1.135	0.0063	0.148	0.0	4.2
0.6	0.446	1.22	0.0145	0.119	0.037	10.0
0.7	0.446	1.175	0.0227	0.102	0.047	15.90
0.8	0.446	1.087	0.0309	0.100	0.047	21.5
0.9	0.446	0.995	0.0391	0.100	0.038	26.3
1.0	0.446	0.905	0.0473	0.100	0.02	30.0

R_P, Tip radius
C, Chordlength
P, Pitch
I_T, total rake, axial displacement of blade sections relative to propeller centerline
T, Blade section thickness
F, Blade section camber
θ_s, Blade section skew, angular displacement of blade sections relative to blade line perpendicular to the hub

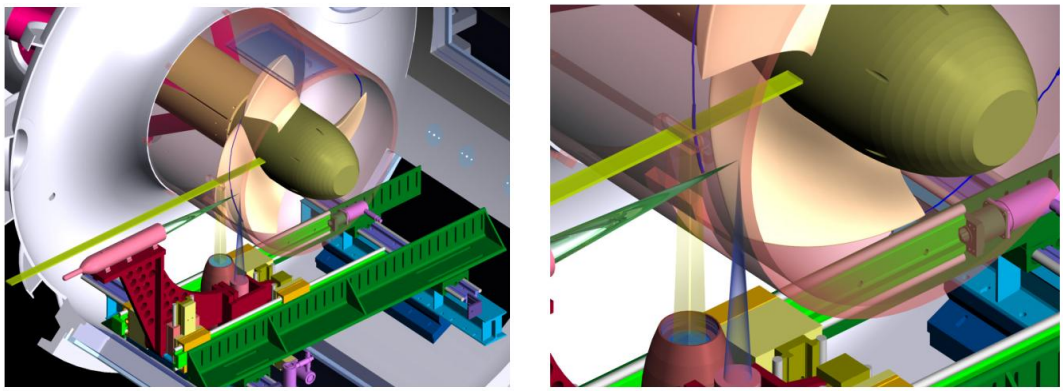

Figure 2: A drawing of the propeller with the duct, LDV system, PIV system, and vortex trajectory. Note the LDV laser beams and the PIV laser sheet and camera. The camera is looking up perpendicular to the laser sheet. The camera mount is on the same traverse as the LDV lasers.

Test Conditions Operation of the propeller poses interesting challenges due to its large size and its complete blockage of the test section flow. Under initial operation of the propeller, attempts to run at its design advance coefficient of $J = 0.75$ required completely shutting down the water tunnel impeller. At around 500 rpm, the rotor mass flow was such that the impeller would begin to free wheel, reducing the flow restriction of the stationary impeller blades and thus dropping the measured rotor thrust and torque. A unique feature of the 36-inch Water Tunnel is the controllable pitch impeller blade, which permits impeller operation over various speeds and blade pitch. It was found that by reducing the pitch of the impeller blades to around zero,

the tunnel flow could be controlled, enabling the rotor to operate over a relatively large range of advance coefficients, $0.65 < J < 1.0$. The standard test conditions at 500 rpm, the highest speed tested, was as follows in the table below. The inlet pressure was maintained high enough (45 psia for 500 rpm) during the LDV and PIV measurements to suppress cavitation.

Table 2. Measured flow conditions.

RPM	Advance Coefficient, J	Velocity ft/s (m/s)	Thrust lbs (kN)	Torque ft-lbs (N-m)	K_T	K_Q	$Re_{0.7}$
500	0.972	22.85 (6.89)	2560 (11.39)	1280 (1735)	0.314	0.056	7×10^6

The operating advance coefficient was selected to produce a typical leakage vortex, without unwanted flow conditions over the blade. The operating $J = 0.971$ was increased relative to design $J = 0.75$ to avoid the formation of the leakage vortex at the leading edge. Additional increase in J was avoided to prevent the occurrence of pressure side leading edge cavitation near the blade tip.

High-Speed Video Camera Photos of the cavitating vortex were taken with a Broadcast quality, Sony Digital Betacam camera. Examples of the cavitating vortex are shown in Figures 12 and 13.

Laser Doppler Velocimetry An all fiber-optic LDV system allowed for three component velocity measurements. The measurement volume was positioned at a point in the horizontal plane containing the propeller axis. The probe volumes are ellipsoidal, 0.7 x 0.7 x 1.3 mm. The probe volumes for the axial and tangential components are coincident, and are oriented with the long axis on a radial line. The probe volume for the radial component is perpendicular to the other two volumes, with the long axis on a tangential line.

LDV measurements were taken upstream and downstream of the rotor. A window upstream of the rotor permitted the measurement of axial and tangential velocities along a radial line upstream of the rotor. Figure 2 shows the windows installed in the shroud to permit measurement of the tip-leakage flow. Three velocity components were measured. The position of the shaft was encoded with an 8192 counts/revolution signal, which was recorded with each velocity measurement. The measurements are grouped into 1024 circumferential positions, each 8 encoder counts wide. At each measurement point, 300,000 velocity measurements were made. This means that each component of each vector on a plot respresents approximately 100 velocity measurements. Doppler signals were analyzed with a TSI Model IFA 655 Digital Burst Correlator. The processor performs a 256-sample, double-clipped, autocorrelation on each Doppler burst, allowing the measurement of velocity even when the signal-to-noise ratio is low. The processors were operated in the random mode. The fiber-optic LDV system consisted of two 3.25 inch TSI model 9832 fiber optic probes. The two probes were rigidly mounted together on a traverse that could translate in the axial and radial directions. The horizontal probe utilized the green (514.5 nm) and violet (476.5 nm) beams of the argon-ion laser to measure the tangential and axial components of velocity, respectively. The vertical probe utilized the blue (488 nm) beam of the argon-ion laser to measure the radial component of velocity.

Particle Image Velocimetry The PIV measurements were made using two Quanta-Ray PRO-Series Pulsed Nd:YAG lasers rated at 800 mJ/pulse output at 532 nm. The laser output was formed into a light sheet of 5 mm thickness. The light sheet passed through windows in the water tunnel and duct to illuminate the flow, and the sheet was oriented parallel to the propeller-shaft axis (Figure 2). The axial position of the camera and sheet were moved to place the mean center of the vortex in the center of the image. Silcon Carbide particles of mean diameter 1 μm were added the flow. A LaVision Flowmaster 3S PIV/PTV system was used to control the firing of the lasers and synchronize image capture with a digital imager, a 1280 x 1024 pixel cross-correlating camera with 12 bit resolution. The camera axis was perpendicular to the laser sheet and recorded the in-plane motion of the tracer particles. The light sheet was sufficiently thick to reduced the number of particles that entered or exited the light sheet due to strong cross-plane flow velocities. The camera was contained in a water-proof housing within the test section of the water tunnel.

The image field-of-view was 24 by 30 mm, and the lenses on the camera were chosen to have a depth-of-field much larger than the thickness of the light sheet. The PIV images were spatially calibrated by taking images of a registration target in the image plane. Images of the target were taken in the filled test section.

The double pulsed PIV images were analyzed using the LaVision software DaVis version 5.4.4. An adaptive multi-pass image process was employed starting with interogation windows of 64 x 64 pixels and

repeating with a final interrogation windows of 32 x 32 pixels. The spatial resolution of the velocity vector field is 0.75 mm. There were typically fewer than 10% bad vectors before postprocessing. A three-by-three gaussian smoothing filter was used on the vector fields. Averages were calculated from 532 individual PIV images.

With the advantage of the high spatial resolution of the PIV vector fields, it was possible to assess the vortex characteristics such as its core radius by direct measurement. The core radius was defined as the radius of a circle with an area equivalent to that enclosed by the polygon centered at the point of minimum speed and formed by the points of maximum speed magnitude positions (core contour). We will refer to the average value of these maximum speeds as the tangential speeds, V_t. The maximum tangential speed value on the core contour is denoted $V_{t_{max}}$. The strength of the vortex was calculated by integrating the vorticity vector over the core area. The vorticity vector at each cell (square) was calculated from the following formula, $w_z = (\oint_c \vec{u} \cdot d\vec{l})/(\oint_c dA)$; which is the circulation, or the line integral of the velocity around a closed path, c, enclosing the cell, divided by the area enclosed by c. The path c is a concentric square with the cell of interest and having twice the side length. The velocities from the eight neighboring cells, four at the sides and four at the corners of the cell under consideration were involved in the calculation. The area enclosed by the path c was made up of the area of the cell under consideration plus 1/2 the area of the four side cells plus 1/4 the area of the four corner cells. Three methods of vector field averaging are presented below: simple-averaging, center-averaging based on the location of minimum speed near the vortex core, and center-averaging based on the position of maximum vorticity near the vortex core.

3 Flow Upstream of the Rotor

Figure 3 shows the axial and tangential flow upstream of the rotor. The flow was measured at $x/R_P = -0.362$ where x is measured along the axial flow direction, and $x = 0$ corresponds to the center of the 12-inch (0.3048 m) long propeller hub. R_P is the radius of the rotor. The LDV velocity measurements were non-coincident and taken at various radial positions. The advance coefficient was $J = 0.983$ and data was taken at 250 and 500 rpm. U_x is the velocity in the axial direction, U_t is the tangential velocity, and U_0 is the tunnel flow velocity. The black line shows the axial velocity, the red line shows the tangential velocity, the solid points are for 250 rpm, and the outlined points are for 500 rpm. The boundary layers on the duct and on the hub can be seen. The duct boundary layer has a thickness of about $0.07R_P$. This corresponds to about 5 times the tip-clearance dimension. The tangential velocities are nearly zero near the tip.

4 Average Tip-Leakage Vortex Flow

LDV and PIV were used to measure the average flow near the tip of the blade. Presented here are planar velocity fields. The plane is parallel to the axis and corresponds to an axial distance $\Delta x/R_P = 0.071$ and to the radial distance $\Delta r/R_P = 0.056$. The axial position was moved to center the vortex for images taken at different blade delays. As the rotating blade passes through this plane, the tip-leakage vortex intersects the image plane, and the axis of the vortex is almost perpendicular to the plane.

Figure 4 shows a schematic diagram of the LDV and PIV vector fields with respect to the duct wall and the propeller blade. The images are taken such that the blade is moving into the paper. The leakage vortex is moving from the pressure side of the blade to the suction side showing a counterclockwise rotation when viewed from below (as the PIV camera imaged the flow.). The duct is at the top of the image and the mean tunnel flow is moving from left to right through the plane. The angular position of the rotor, θ, is measured with respect to this plane. When θ equals zero, the trailing edge of the blade intersects the plane, and as θ increases, the blade moves farther away. This distance is presented as $S = \theta R/C$ where C is the chord of the blade.

It is interesting to compare the average flow fields measured with LDV and PIV. Figure 5 presents velocity fields measured with LDV, on the left, and PIV, on the right. The LDV is shown with only 2-components of velocity for comparison with the PIV. The PIV has been simple-averaged over 532 images for comparison with LDV measurements. The PIV velocity field shows good spatial resolution and matches the LDV measurements.

Propulsor Inflow at 250 and 500 rpm

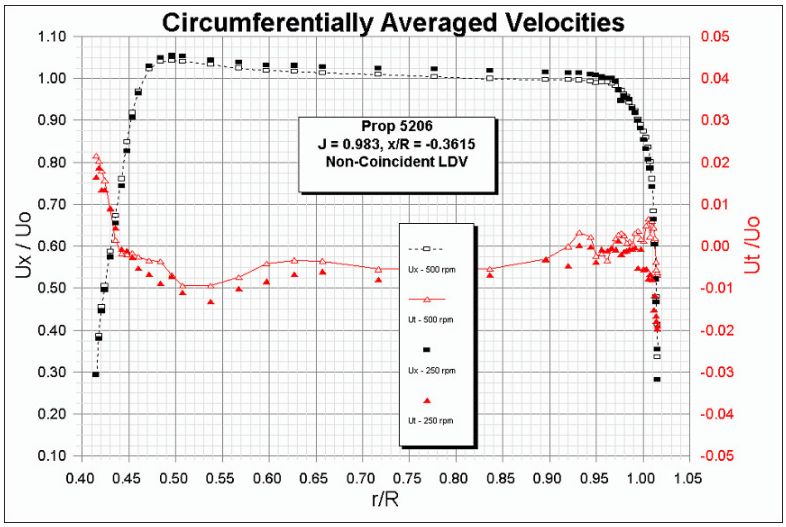

Figure 3: Upstream non-coincident LDV velocity measurements at various radial positions at an advance coefficient of $J = 0.983$and at an axial location of $x/R_P = -0.3615$. U_x is the velocity in the axial direction, U_t is the tangential velocity, and U_0 is the tunnel flow velocity. These measurements were taken at 500 and 250 rpm. The black line is the axial velocity and the red line is the tangential velocity. The solid points are for 250 rpm and the outlined points are for 500 rpm.

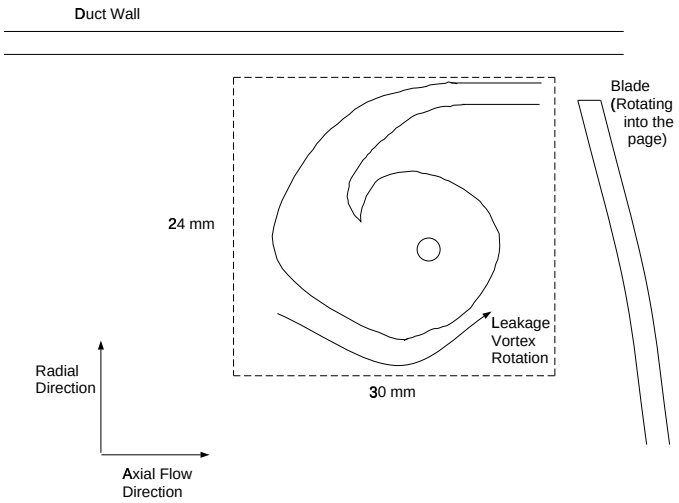

Figure 4: Schematic diagram of LDV and PIV velocity fields. Note that the images are taken such that the blade is moving into the paper (see Figure 2).

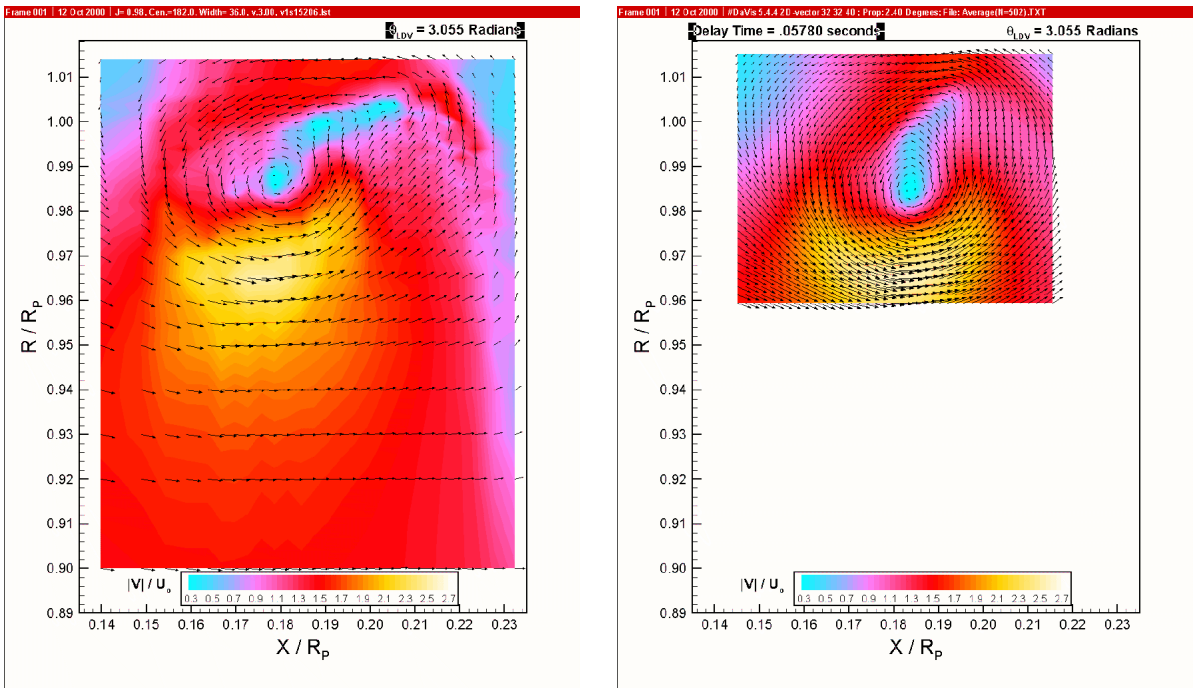

Figure 5: LDV and PIV velocity vectors for S=0.0296 at 500 rpm and 45 psia. The contour color shows the vector magnitude. x/R_P is the non-dimensional distance in the axial direction and r/R_P is the non-dimensional distance in the radial direction. The PIV is averaged over 532 images. The LDV is shown with only 2-components of velocity for comparison with the PIV. The LDV has a covers a larger domain, but the PIV shows good spatial resolution and matches the LDV velocity measurements.

It is important to remember that the vortical flow near the trailing edge is typically three dimensional, and that the PIV image is only a two-dimensional cut of this flow averaged across the PIV imaging light sheet. This is illustrated in Figure 6. Here a comparison is made between 2-component and 3-component LDV measurements. On the left is a 2-component velocity field parallel to the PIV measurement plane. On the right is the velocity field of a plane that was slightly tilted. Because the vortex does not necessarily cut the PIV measurement plane at a right angle, the vortex on the left appears less axially symmetric. The axial symmetry is recovered after tilting the plane. Consequently, it is important not to interpret the PIV images as perpendicular cuts of a two-dimensional vortex. The PIV imaging plane remained parallel to the axial flow direction, and the vortex may not intersect it at a right angle.

5 Variability of the Tip-Leakage Vortex Flow

While only a 2-dimensional realization of the flow, the advantage of the PIV visualization is the possibility of capturing many instantaneous flow fields. The tip leakage flow is highly unsteady, as evidenced by the variation in single PIV images. Figure 7 shows four PIV images taken at the same operating conditions and downstream location. All vector plots are for the same blade angles or blade positions, the trailing edge is 1.52^o ($S = 0.0296$) and 27.02^o ($S = 0.5259$) above the plane of measurement. Variation in the flow field can be readily observed. The position, strength, and core size of the vortex varies between images. The contours show changes in the measured out-of-plane vorticity.

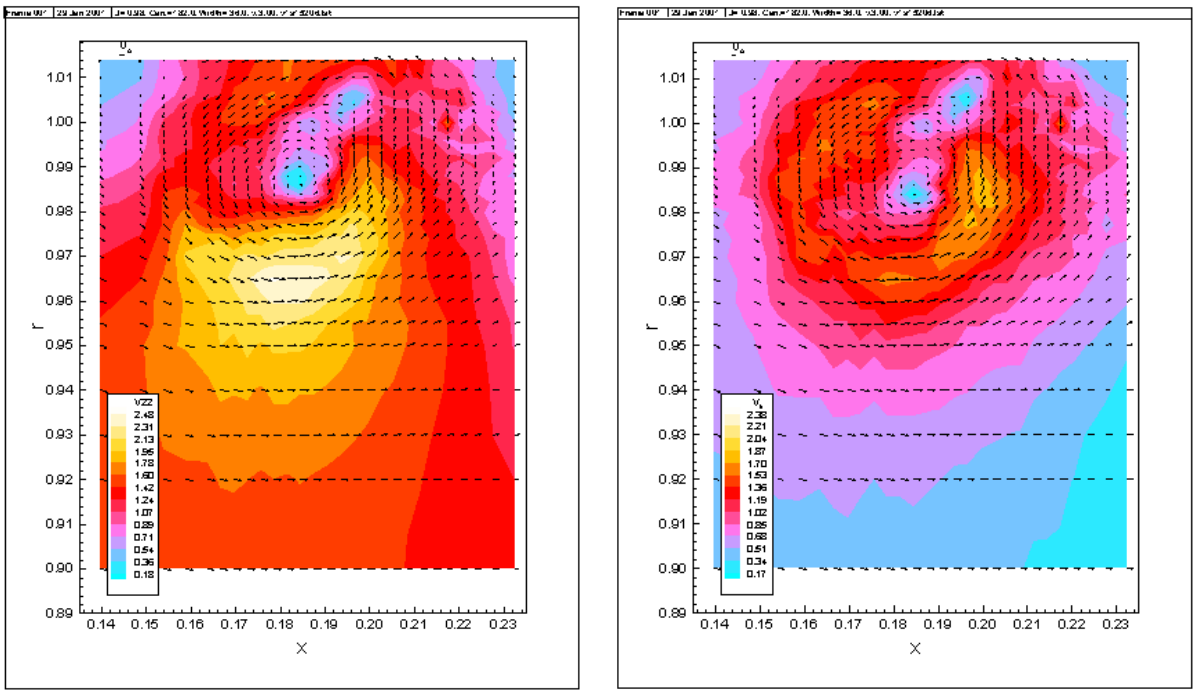

Figure 6: 2-component versus 3-component LDV measurements. These measurements were taken at 500 rpm, 45 psia, and S=0.0296. The 2-component LDV gives similar results to the simple-averaged PIV. The contour color corresponds to vector length. The 3-component measurements result in a more accurate mean core structure of the vortex. The vortex is not necessarily oriented with the horizontal plane. The 3-component LDV measurements allow a non-horizontal cut to be taken so that the vortex is perpendicular to the in-plane velocity measurements. r/R_P and x/R_P are shown.

Table 3. Comparison between simple-averaged PIV and center-averaged PIV vortex quantities.

S	Type of average	Radius, a (mm)	Circulation, Γ (m^2/s)	$-(\frac{\Gamma}{2\pi a})^2$ $(m/s)^2$	Average tangential velocity, V_t (m/s)	Maximum tangential velocity, $V_{t_{max}}$ (m/s)
0.0296	simple average	8.695	-0.7146	-171.1	13.16	18.01
0.0296	velocity centered average	8.511	-0.7026	-172.6	13.14	17.90
0.0296	vorticity centered average	8.630	-0.7034	-168.3	13.12	17.85
0.5259	simple average	12.62	-0.6193	-61.02	8.506	11.32
0.5259	velocity centered average	12.27	-0.6024	-61.06	8.440	11.12
0.5259	vorticity centered average	12.74	-0.5885	-54.03	8.060	10.56

Figure 11 shows histograms of the vortex-center location for S = 0.0296 and S = 0.5259. The location of the vortex core varied by ±1 mm and ±3 mm, respectively, or 11% and 26% of the vortex core radii. After identifying the position of the vortex, it is possible to shift the PIV images so that a centered-average can be computed. Table 3 shows three averages computed for 532 PIV images. The simple-average is just the non-shifted average of the PIV images. The velocity-centered average used the position of minimum velocity near the vortex core as the locus for the average, and the vorticity-centered average used the position of maximum vorticity near the vortex core. Figure 9 shows the averaged PIV images for these two blade values, S. For the case of S = 0.0296, the effect of vortex wandering is small, with changes in the core size of the centered-averages less than 2% compared to the simple-average. The wandering is greater for the case of $S = 0.5259$, with the differences approaching 3%. These results are consistent with the calculations of Straka and Farrell (1992). They computed the effect of vortex wandering on the resulting averaged flow field of a two-dimensional Burgers vortex and showed that the amplitude of vortex must wander by greater 50% of the core radius for the simple-average measurement to depart from the center-averaged measurement.

Figure 11 presents histograms of the core radius, a, the circulation around the viscous core, Γ, the average tangential speed, V_t, the maximum value for the tangential speed, $V_{t_{max}}$, and the quantity $-(\Gamma/2\pi a)^2$, for two blade angles. For S = 0.0296, the core radius ranges between 7.40 and 10.12 mm, the average circulation is between -0.82 and -0.66 m^2/s, and the average tangential velocities were between 12.82 and 14.96 m/s with the maximum tangential velocities between 16.66 and 21.01 m/s.

As discussed above, variation in the angle that the vortex axis makes with the PIV light-sheet can lead to variation in the measured quantities of the vortex. Consider a line vortex with radius a_0 that makes an angle of α with the PIV plane. The vortex core will be imaged as an ellipse with area $\pi a_0^2 \sec(\alpha)$. The measured average core diameter would then be larger than the actual core diameter by a factor of $(\sec(\alpha))^{1/2}$. A 10^o variation in the incidence angle will result in a 1% increase in the measured core size, and a 20^o inclination will result in a 3% variation. The actual angle of incidence is likely to be much less than $\pm 20^o$. Consequently, the observed variability in the instantaneous PIV quantities is not principally due to vortex wandering but is the result of true variations in strength and size of the vortex.

6 Development of the Tip-Leakage Vortex Flow Downstream of the Blade

The vortex core size and strength vary as the vortex flow moves downstream of the blade trailing edge. Figure 10 shows these quantities plotted as a function of S. Variation of these curves are relatively smooth, except for the region just downstream of the trailing edge where the leakage vortex is rolling up and may be interacting with a trailing edge vortex. For S > 0.2312 the variation is quite smooth. The radius of the core size increases as the blade moves up and away from the plane of measurement. The circulation shows a generally increasing trend as the trailing edge moves further out of the plane of measurement. The average tangential velocity and the maximum tangential velocity show a peak right when the trailing edge of the blade is in the plane of measurement ($S = 0$) and then decrease as the blade moves further away. Lastly, the quantity $(\Gamma/2\pi a)^2$ is largest near the trailing edge and is reduced farther downstream. These data can also be derived from the 3-dimensional LDV data, along with the axial velocity within the vortex core. We intend to compare the PIV and LDV results more closely.

7 Developed Tip-Leakage Vortex Cavitation

The cavitating vortex core was visualized by reducing pressure beyond inception, as shown in Figures 12 and 13. Visualization of the vortex shows that it is angled relative to the PIV plane by approximately 15^o in the upstream axial direction near the trailing edge and about 3^o upstream of the trailing edge. Surface cavitation can be observed in the gap region for the developed cavitation. High-speed video showed wandering of the vortex with a displacement that ranged from very little when the vortex was a along side of the blade (less then one-half the core width) to 100% of the observed vapor core diameter about 0.1524 m (6in) downstream. This is consistent with the wandering amplitude of the non-cavitating vortex. Downstream of that the vortex wanders more, probably due to the combining on the trailing edge vortex and general wake roll up. At this

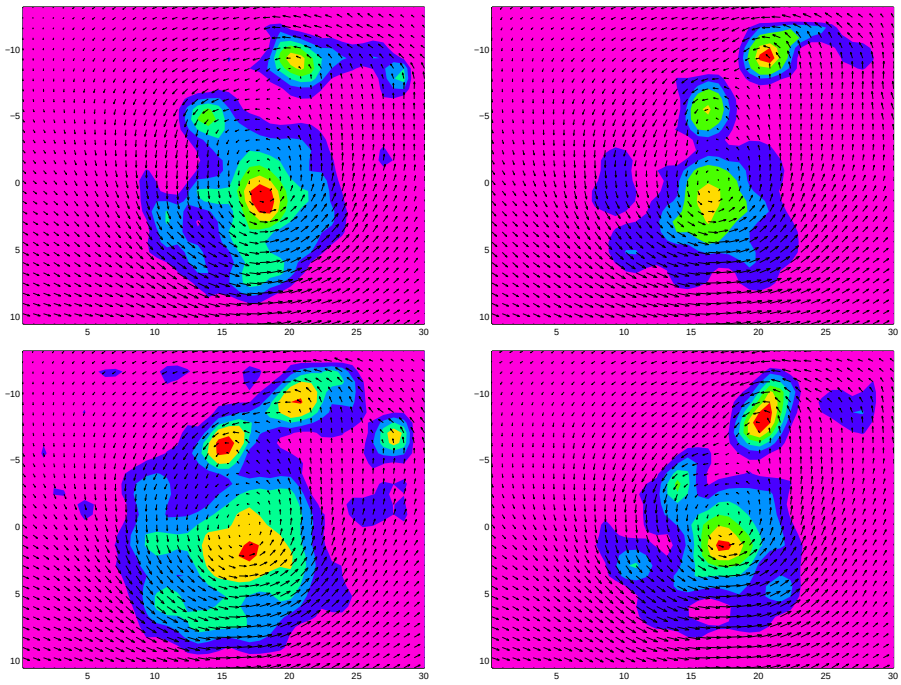

S=0.0296

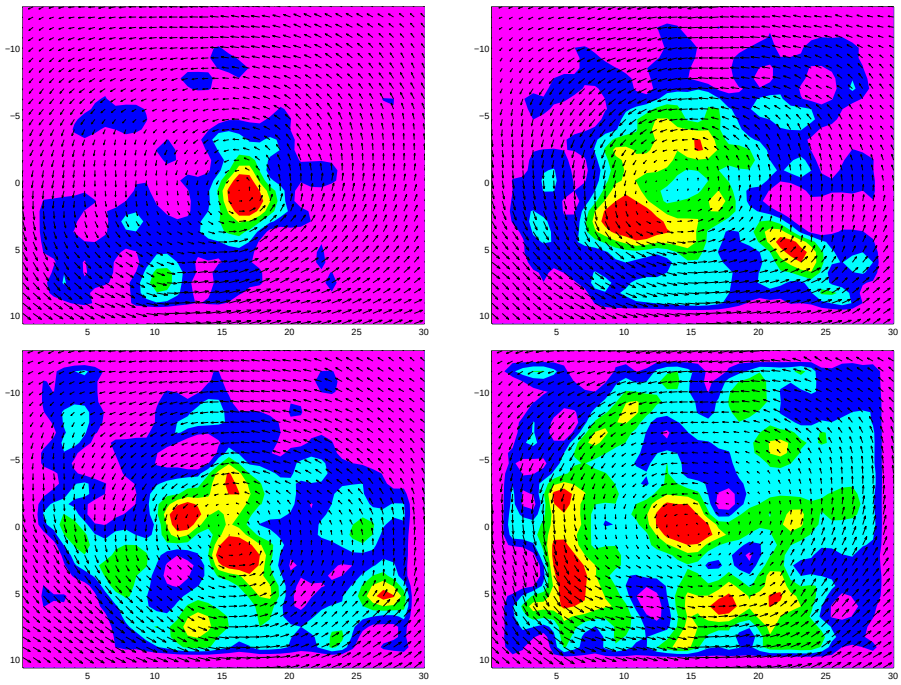

S=0.5259

Figure 7: Four instantaneous PIV images taken at S=0.0296 and S=0.5259, 500 rpm, 45 psia. Velocity vectors are shown with contours of vorticity. The vortex center and vorticity changes with each image.

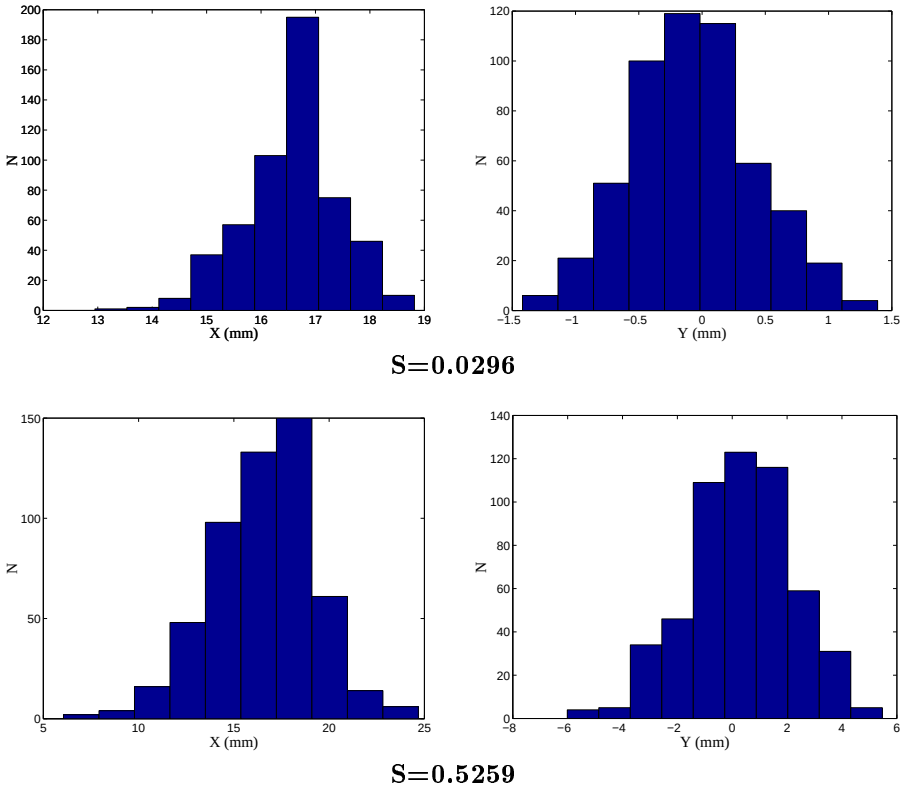

Figure 8: Histograms of the (X,Y) position of the vortex center showing the amount of wandering at S=0.0296 and S=0.5259, 500 rpm and 45 psia. The PIV measured the vortex core over a range of 5.36 (mm) in the x-direction and 3.06 (mm) in the y-direction for $S = 0.0296$. The wandering increases further from the blade.

point the vortex gets much more distorted and wanders up to 300% of the observed vapor core.

Arndt and Keller (1992) employed the principal of angular momentum conservation to show that the diameter of the vapor core of a developed cavitating Rankine vortex is smaller than the non-cavitating vortex core by a factor of $1/\sqrt{2}$. Here the non-cavitating core radius was measured to be 9 mm downstream of the trailing edge, and the measured vapor core had a radius of approximately 3 mm, or 0.3 times the original core radius. This is much lower than the expected value of $1/\sqrt{2} = 0.71$. Similar measurements of the cavitating to non-cavitating core ratio for tip vortex forming on a stationary elliptic hydrofoil yielded a ratio of 0.5 (Briançon-Marjollet and Merle, 1997).

Figure 13 shows a detail of the leakage vortex, where surface cavitation at the tip convects into the vortex. The flow direction can be observed along with the increase in cavitating vorticity, fed by the gap flow.

8 Conclusions

The tip-leakage vortex occurring on a ducted rotor was examined using both LDV and PIV. Preliminary analysis of the data indicates that the there is substantial variability in the instantaneous vortex quantities, such as the size of the viscous core and the strength of the vortex. Inception of discreet cavitation events will occur when nuclei are captured within the vortex, experience tension, and vaporously grow. Inception can occur when an unusually large nucleus is captured by the average vortex, and when an average nucleus is captured by an unusually strong vortex. We are presently conducting inception experiments to determine how variability of the vortex influences inception of discreet cavitation events. We will examine when and where discreet cavitation events occur, and attmpt to relate this to the measured two- and three-dimensional

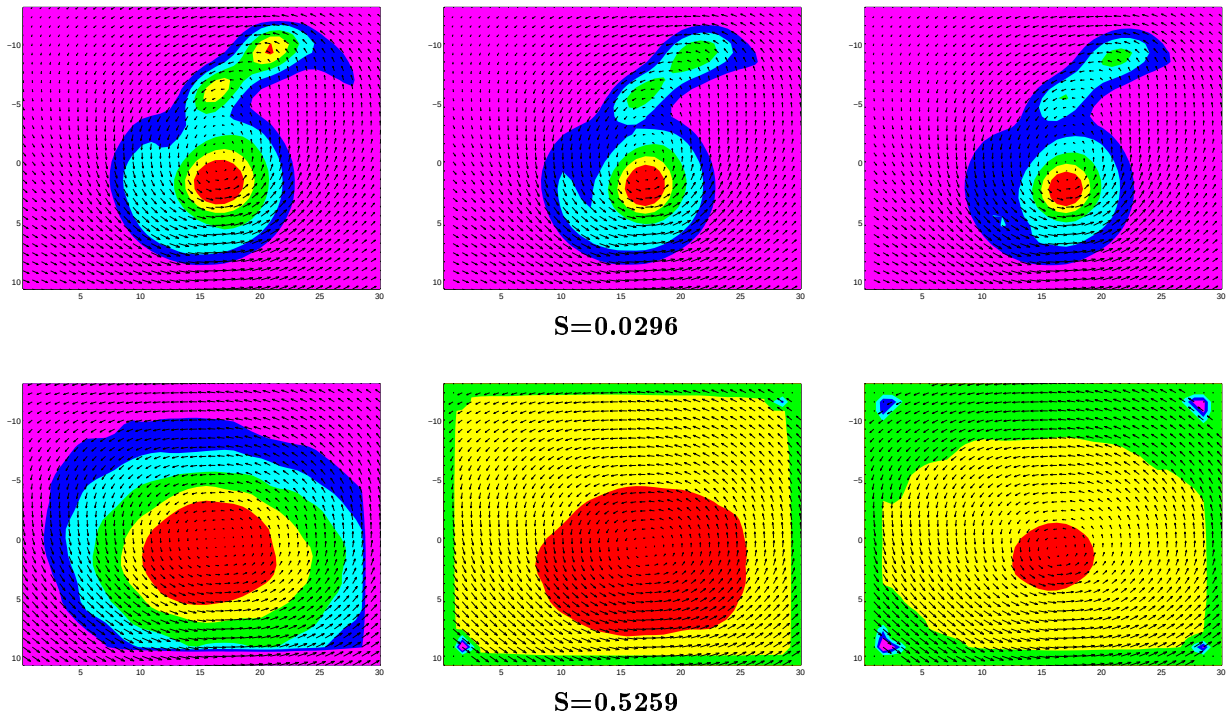

Figure 9: Averaged and centered-averaged velocity vectors and vorticity contours from 532 PIV images at 500 rpm, 45 psia, and S = 0.0296 and 0.5259. An average where the center of each vortex is in the same location is called 'centered-average'. The simple-averaged image shows a larger vortex core size and lower tangential velocities. Table 3 shows variations in vortex quantities between the two averaging methods.

flow quantities.

Acknowledgements

This work was sponsored by the Office of Naval Research, performed by the Carderock Division of the Naval Surface Warfare Center, Code 5400 and the University of Michigan under ONR contract N00014-99-1-0307.

References

Ardnt, E., A. and Keller, A. P. (1992). *Journal of Fluids Engineering.*, **114**, 430-438.

Boulon, O., Callanaere, M., Franc, J.-P., and Michel, J.-M. (1999). *Journal of Fluid Mechanics.*, **390**, 1-23.

Brennen, C.E. (1995). *Cavitation and bubble dynamics*, Oxford Univ. Press.

Briançon-Marjolet, L. and Merle, L. (1997). 21^{st} *Symposium on Naval Hydrodynamics.*, 851-864.

Brownell, W. F. (1962) *DTMB Report 1690*

Chesnakas, C. and Jessup, S. (1998). 22^{rd} *Symposium on Naval Hydrodynamics.*, 139-152.

Farrell, K. J. and Billet, M. L. (1994). *Journal of Fluids Engineering.*, **398**, 1-43.

Fruman, D., Dugué, C., Pauchet, A., Cerruti, P., and Briançon-Marjolet, L. (1992). 19^{th} *Symposium on Naval Hydrodynamics.*, 633-654.

Fruman, D.H., Pichon, T., and Cerruti, P. (1995). *Journal of Marine Science Technology.*, **1**, 13-23.

Gopalan, S., Liu, H., and Katz, J. (2000). 23^{rd} *Symposium on Naval Hydrodynamics.*, 177-187.

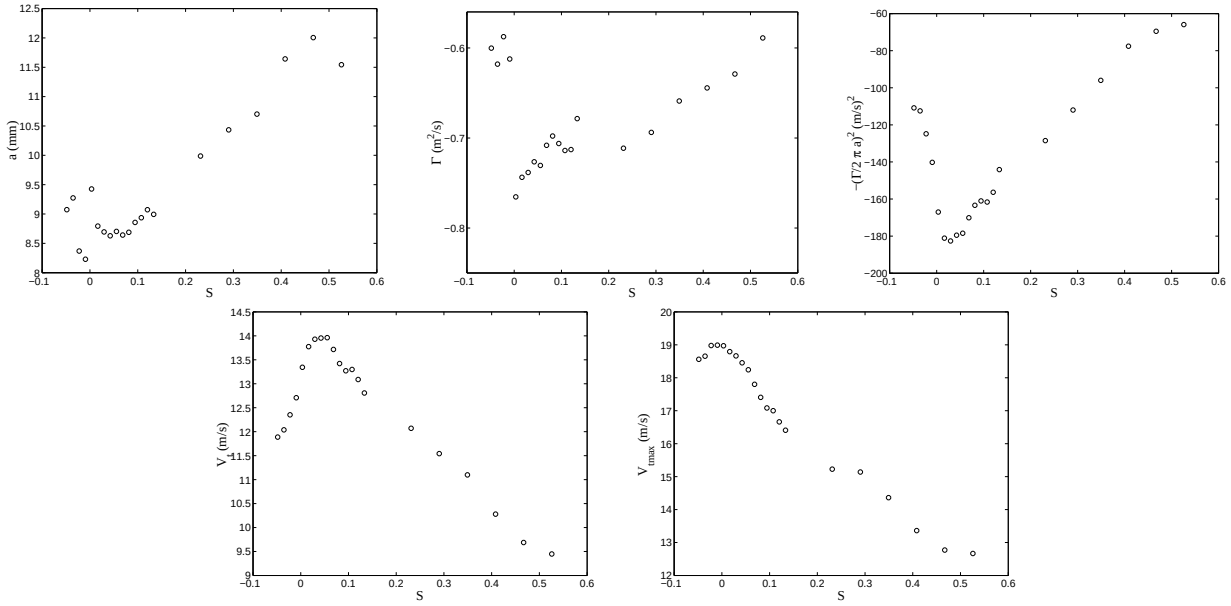

Figure 10: Distributions of radius (a), circulation (Γ), average tangential velocity (V_t), maximum tangential velocity ($V_{t_{max}}$), and the quantity $-(\Gamma/2\pi a)^2$ for 532 PIV images at various non-dimensional S locations at 500 rpm and 45 psia. S is the non-dimensional circumferential distance the trailing edge of the blade has traveled. It is non-dimensionalized by the chord-length.

Maines, B. H. and Arndt, R. E. A. (1997). *Journal of Fluids Engineering.*, **119**, 413-419.

McCormick, B. W. (1962). *ASME Journal of basic Engineering.*, Sept., 369-379

Pauchet, A. (1997). 21^{st} *Symposium on Naval Hydrodynamics.*, 865-881.

Straka, W. A. and Farrell, K. J. (1992). *Experiments in Fluids.*, **13**, 163-170.

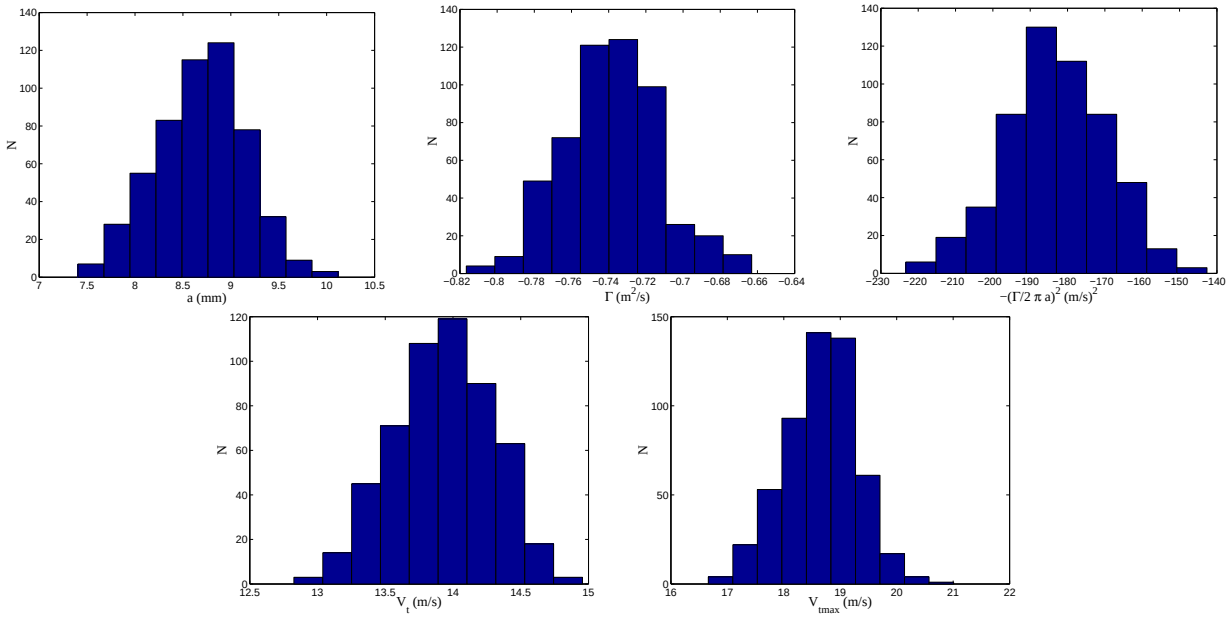

S=0.0296

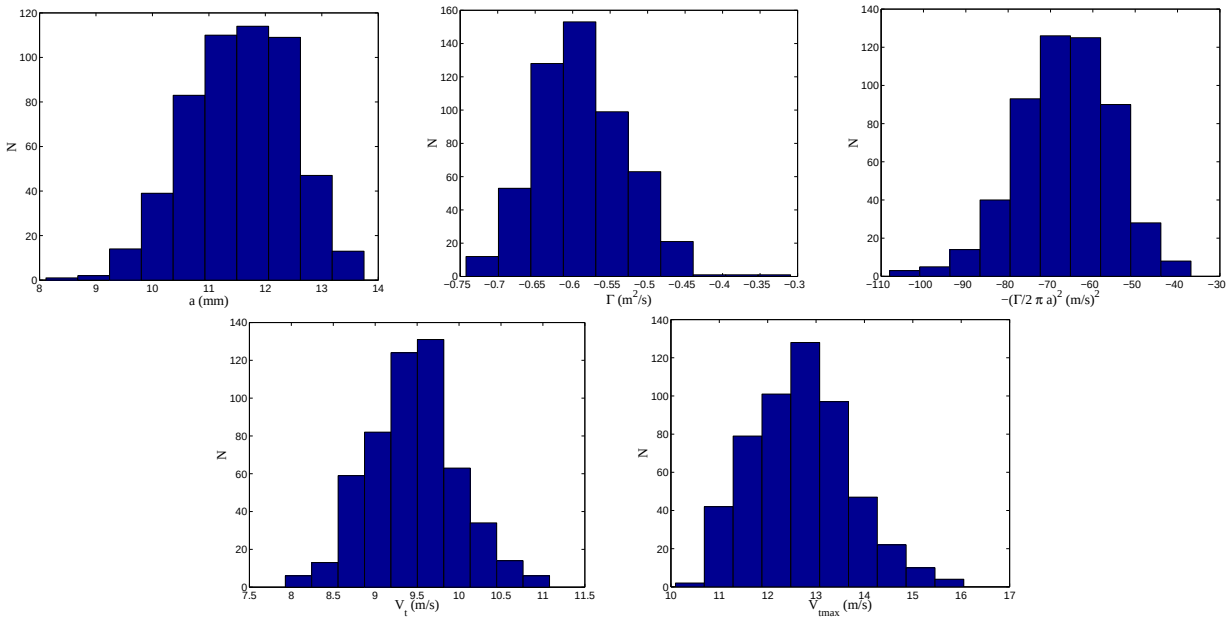

S=0.5259

Figure 11: Distributions of radius (R), circulation (Γ), average tangential velocity (V_t), maximum tangential velocity ($V_{t_{max}}$), and the quantity $-(\Gamma/2\pi a)^2$ for 532 PIV images for S=0.0296 and S=0.5259 at 500 rpm, 45 psia. Note the variation in vortex quantities for a single blade angle.

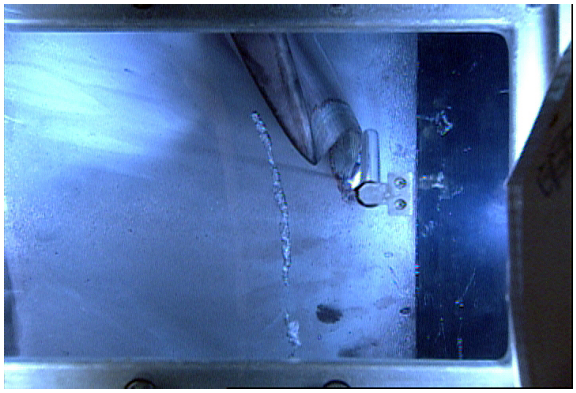

Figure 12: Photo of the cavitating vortex at 500 rpm and pressure at 25 psia. The cavitating vortex core is visualized by reducing the pressure beyond inception.

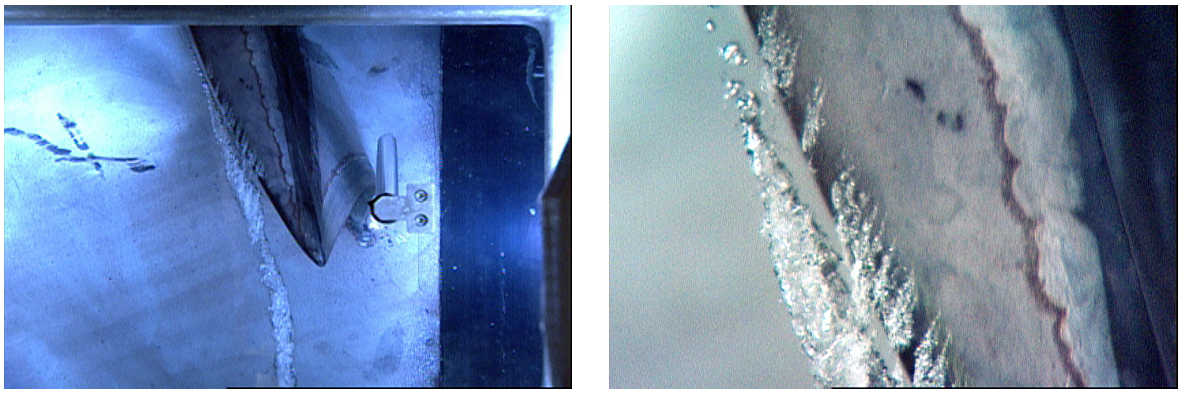

Figure 13: Photo of the cavitating vortex near the blade at 500 rpm and pressure at 18 psia with a close up of the surface cavitation. Note where the surface cavitation at the tip convects into the vortex.